Large oxygen excess in the primitive mantle could be the source of the Great Oxygenation Event

Denis Andrault, Manuel Muñoz, Giacomo Pesce, Valerio Cerantola, A. Chumakov, I. Kantor, S . Pascarelli, R. Rüffer, L. Hennet

Geochemical Perspectives Letters

Large oxygen excess in the primitive mantle could be the source of the Great Oxygenation Event

D. Andrault[1*], M. Muñoz[2], G. Pesce[1], V. Cerantola[3], A. Chumakov[3], I. Kantor[3], S. Pascarelli[3], R. Rüffer[3], L. Hennet[4]

OPEN ACCESS

doi: 10.7185/geochemlet.1801

Abstract

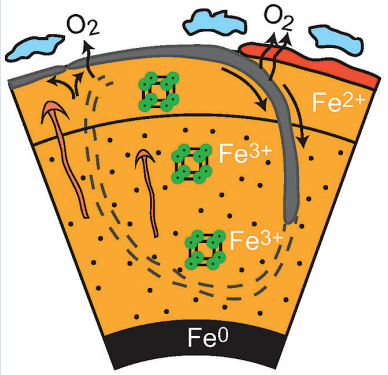

Before the Archean to Proterozoic Transition (APT) the tectonic regime was dominated by microplates floating on a low viscosity mantle. Such a regime restricted chemical exchange between the shallow and deeper mantle reservoirs. After the APT, a more global convection regime led to deep subduction of slabs. We propose that the improved vertical mixing of the mantle favoured the release to the Earth's surface of an oxygen excess initially trapped in the deep mantle. This excess built up when the primordial lower mantle was left with a high $Fe^{3+}/(Fe^{2+}+Fe^{3+})$ ratio ($\#Fe^{3+}$), after metallic iron segregated down into the core. Our synchrotron-based *in situ* experiments suggest a primordial Fe^{3+}excess of ~20 % for the mantle iron. By comparison with the $\#Fe^{3+}$ of the present mantle, this Fe^{3+}excess would correspond to 500–1000 times the O_2 content in the Earth's atmosphere. The tectonic transition greatly facilitated the ascent of oxidised lower mantle material towards the Earth's surface, inducing a continuous arrival of O_2 at the Earth's surface and into the atmosphere.

Received 31 July 2017 | Accepted 14 December 2017 | Published 18 January 2018

Introduction

The main lower mantle phase, bridgmanite (Bg: (Mg,Fe)(Si,Al)O_3) can easily incorporate Fe^{3+}. This effect is related to a strong coupling of Fe^{3+} and Al^{3+} cations on the A and B sites of the ABO_3 perovskite-type lattice. The Al-Fe^{3+} interaction in this phase is so favourable that it can induce the disproportionation of Fe^{2+} into Fe^{3+} (which is incorporated into Bg) and metallic iron (Fe^0) (Fig. 1) (Frost *et al.*, 2004). Such electron transfer occurs when a predominantly Fe^{2+}-bearing upper mantle material is buried below the 660 km discontinuity by mantle convection. In the solid lower mantle, the Fe droplets are expected to remain relatively small and separate (Yoshino *et al.*, 2003). Thus, they are gravitationally metastable in the lower mantle. When this mineral mixture migrates upwards to the upper mantle, the coexisting Fe^{3+} and Fe^0 can eventually recombine with each other (*i.e.* $2Fe^{3+} + Fe^0 \rightarrow 3Fe^{2+}$), leading to a dominantly Fe^{2+}-bearing upper mantle with a true Fe^{3+} excess of only 2–3 % (Frost *et al.*, 2008). This ongoing cycle of Fe^{2+} disproportionation followed by Fe^{3+} plus Fe^0 recombination results in a neutral budget of the cation/oxygen ratio of the mantle. It remains difficult, however, to provide quantitative estimates of the $\#Fe^{3+}$ in the deep mantle, because different studies present a controversial range of $\#Fe^{3+}$ values from 10 % to 60 % or more, for pressures up to the 135 GPa found at the core-mantle boundary (see Shim *et al.*, 2017).

The redox equilibrium between Bg with a high $\#Fe^{3+}$ and metallic Fe^0 was established early in the Earth's history. However, the core-mantle segregation induced drainage of Fe^0 droplets from the molten mantle down into the core, which resulted in a large Fe^{3+} excess in the primordial lower mantle (Frost *et al.*, 2008). This excess became a potential source of oxygen for the shallow mantle and the Earth's surface. This is highly important with respect to the Great Oxygenation Event (GOE) which occurred 2.2–2.5 Ga ago (Bekker and Holland, 2012). Different scenarios were proposed to explain the major change in redox state at the Earth's surface at this time, including the emergence of oxygenic cyanobacteria (Buick, 2008), and, in relation to the deep Earth, to a change in the oxidation state of sulphur in volcanic gases (Gaillard *et al.*, 2011). This subject is still hotly debated.

Experimental Determination of the $\#Fe^{3+}$ in the Deep Lower Mantle

Our experiments were aimed at refining the $\#Fe^{3+}$ in the Earth's lower mantle. Starting materials consisted of homogeneous

1. Laboratoire Magmas et Volcans, Université Clermont Auvergne, CNRS-IRD-OPGC, Clermont-Ferrand, France
2. Géosciences Montpellier, Université de Montpellier, CNRS, Montpellier, France
3. European Synchrotron Radiation Facility, ESRF, Grenoble, France
4. Conditions Extrêmes et Matériaux : Haute Température et Irradiation, CNRS, Orléans, France
* Corresponding author (email: denis.andrault@uca.fr)

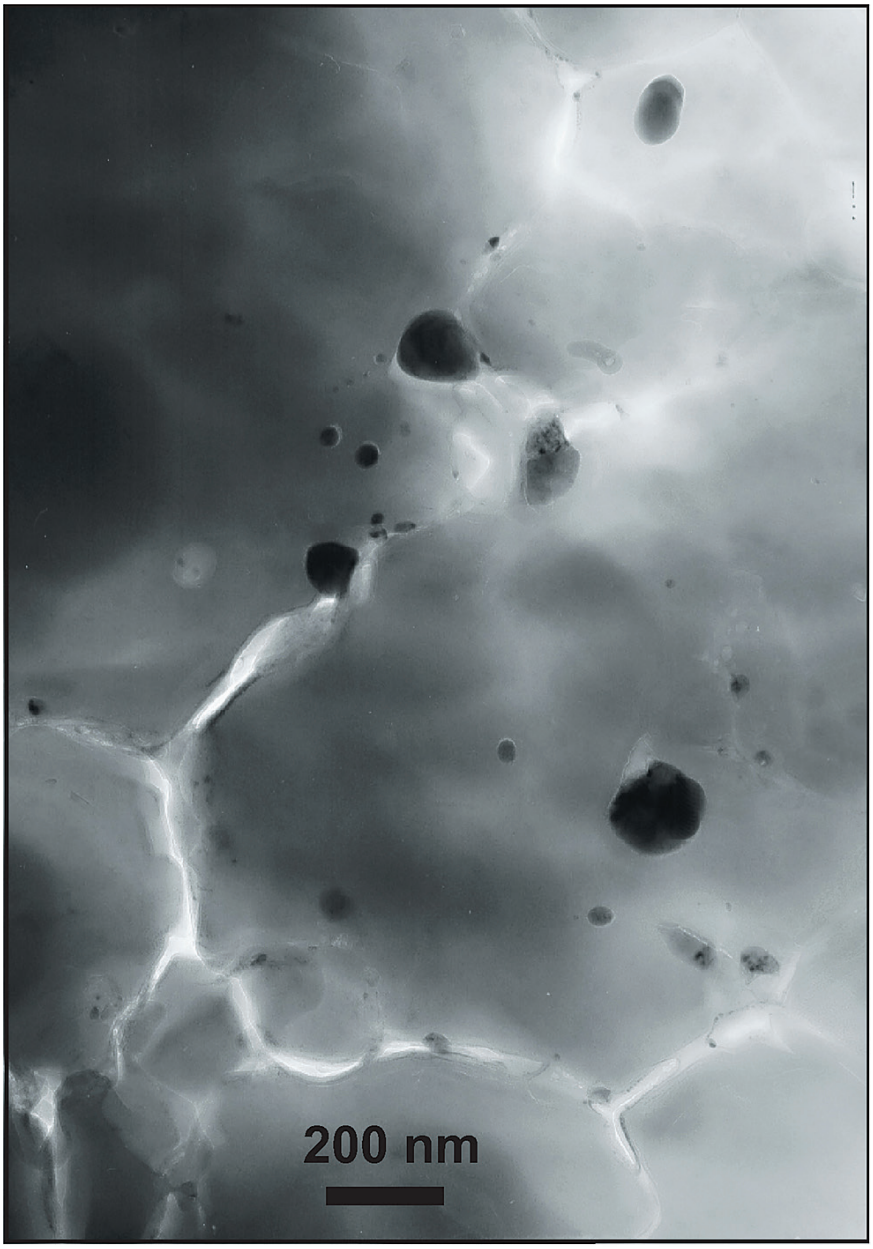

Figure 1 Micrograph of an Al-bearing $(Mg,Fe)SiO_3$ bridgmanite. The starting material consisting of a mixture of $(Mg,Fe)SiO_3$ pyroxene and Al_2O_3 corundum was compressed to 40 GPa and heated to 2500 K, using the LH-DAC. The reaction between the two phases induced the Fe^{2+} disproportionation into a mixture of Fe^{3+}-rich, Al-bearing bridgmanite (large grey areas) and metallic Fe^0 (dark droplets). Early in the Earth's history, core segregation drained the metallic Fe^0 away from the Fe^{3+}-rich Bg, thus leaving the deep mantle with a large oxygen excess.

glasses with a primitive mantle composition, but different Fe and Al contents (Tables S-1 and S-2). Their $\#Fe^{3+}$ was typically 7–8 % (Fig. S-5). Samples were synthesised at P-T conditions ranging from 25 to 140 GPa and 2000 to 3500 K, using a laser-heated diamond-anvil cell (LH-DAC). The DAC provides a closed system in which the cation/oxygen ratio remains constant. This represents a good proxy for natural conditions. During laser heating, chemical segregation associated with temperature gradients was minimised thanks to scanning of the lasers over the sample surface on both sides of the DAC. The valence state of Fe was determined *in situ* using synchrotron-based X-ray absorption (Fe K-edge XANES) and Mossbauer (SMS) spectroscopy (see Supplementary Information).

XANES measurements. We modelled the pre-edge features (Figs. S-1 to S-4, Wilke *et al.*, 2001) to retrieve information on the sample $\#Fe^{3+}$ as a function of pressure. To apply this technique, we first determined the centroid energy position (PCE) of the pre-edge features in two Fp and Bg reference compounds, before comparing them to samples which contained a mixture of both phases. PCEs for both Fp and Bg increase with pressure by 0.3–0.4 eV up to ~30 GPa, before decreasing progressively at higher pressures. Because the iron valence of the reference compounds does not change under compression, such an evolution is likely to be due to pressure effects which are as yet undocumented in the literature.

XANES spectra of our samples (Fig. 2) show PCE values slightly higher than our Bg reference, which suggests an $\#Fe^{3+}$ higher than 27 %, as found in our Bg reference using SMS (Fig. S-6). PCEs of both samples increase regularly with pressure up to more than 120 GPa, in strong contrast with decreasing trends observed for Fp and Bg references. This observation clearly supports a progressive increase in $\#Fe^{3+}$ in CI-NoAl and CI-2Fe samples with increasing pressure.

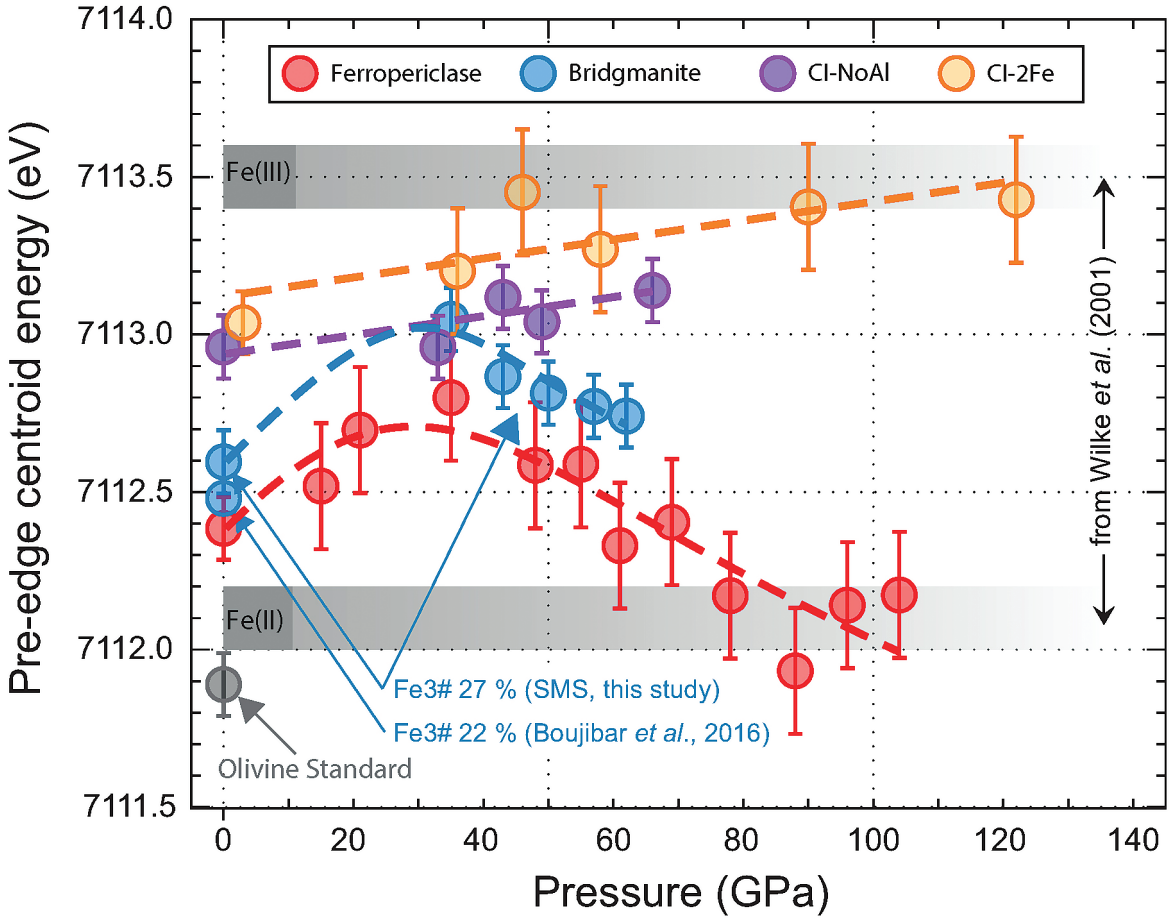

Figure 2 Redox state of Fe probed by X-ray absorption spectroscopy. The pre-edge centroid energy (PCE, Fig. S-4) of our samples (orange and purple dots; see Table S-1) are plotted together with our ferropericlase (red dots, dominantly Fe^{2+}) and bridgmanite (blue dots, 27 % Fe^{3+}) reference compounds. Horizontal grey stripes correspond to PCE values generally found for Fe^{2+} or Fe^{3+}-bearing minerals at ambient P-T conditions (Wilke *et al.*, 2001). PCEs of our samples plot slightly higher than the reference compounds. Also, they increase regularly with pressure, which suggests significant Fe^{3+} contents and excludes a decrease of their bulk #Fe^{3+} up to more than 120 GPa.

SMS measurements. Previous studies present detailed analyses of the main SMS parameters of Fe species located in Bg and Fp (Kantor *et al.*, 2009; Kupenko *et al.*, 2015; Figs. S-7 and S-8). In our sample, which contains a mixture of both phases, we observe an increase in the FeO component in Fp up to ~80 GPa (Fig. 3a), which could be related to the Fe^{2+} spin transition in Fp (Badro *et al.*, 2004). We find a low #Fe^{3+} in our samples synthesised below 30–35 GPa, with #Fe^{3+} similar to those previously reported for Al-free or low-Al Bg phases (Fig. 3b). In this pressure range, Al-rich garnet remains stable (*e.g.*, Irifune *et al.*, 1996), thus inducing a low Al content in Bg. On the other hand, previous SMS measurements performed on a Bg sample containing 6 % Al *per* formula unit suggest #Fe^{3+} of 30–35 % in this pressure range (Kupenko *et al.*, 2015).

Increasing pressure up to ~120 GPa produces a weak and continuous increase in #Fe^{3+} in Bg up to ~40 %. Our measurements are overall compatible with previous work (see Shim *et al.*, 2017 and references therein). At the highest lower mantle pressures, when post-Bg becomes a major component, the bulk mantle #Fe^{3+} becomes 25–30 %, which corresponds to an #Fe^{3+} in the mixture of Bg plus post-Bg of 45–50 %.

Our XANES and SMS analyses are consistent with each other. The more quantitative SMS results yield an average mantle #Fe^{3+} of ~20 % (Fig. 3a). It corresponds to ~2.10^{23} mol of Fe^{3+} in the lower mantle and an excess of ~10^{23} mol of oxygen compared to a predominantly Fe^{2+}-bearing silicate mantle. Today, this oxygen excess is compensated by the presence of ~10^{23} mol of Fe^0 (as in Fig. 1).

An Oxygen Excess Stored in the Primordial Lower Mantle

As mentioned in the introduction, the redox state of the primitive mantle was largely different from that prevailing today, because Fe^0 droplets drained down from the magma ocean into the core. The removal of Fe^0 left the primitive lower mantle with a relative Fe^{3+} excess (Frost *et al.*, 2008), and thus a relative excess of oxygen, compared to the present day mantle. The true oxygen excess in the primitive lower mantle was controlled by two main parameters: (i) the amount of Bg present in the lower mantle when the Fe^0 segregation stopped. Since the magma ocean would have undergone a steep increase in viscosity at 60–70 % fractional crystallisation (Abe, 1997), a transition that would stop the descent of Fe^0 droplets by gravity, we use a Bg fraction of 50 % of the total lower mantle mass to estimate the Fe^{3+} content of the primitive lower mantle at the chemical closure; (ii) the efficiency of Fe^0 droplet segregation. This depends on complex parameters, such as the level of turbulence in the magma ocean. We consider that 50 % of the Fe^0 droplets produced by Bg crystallisation (which induces partial Fe^{2+} disproportionation into Fe^{3+} and Fe^0) were efficiently segregated into the core.

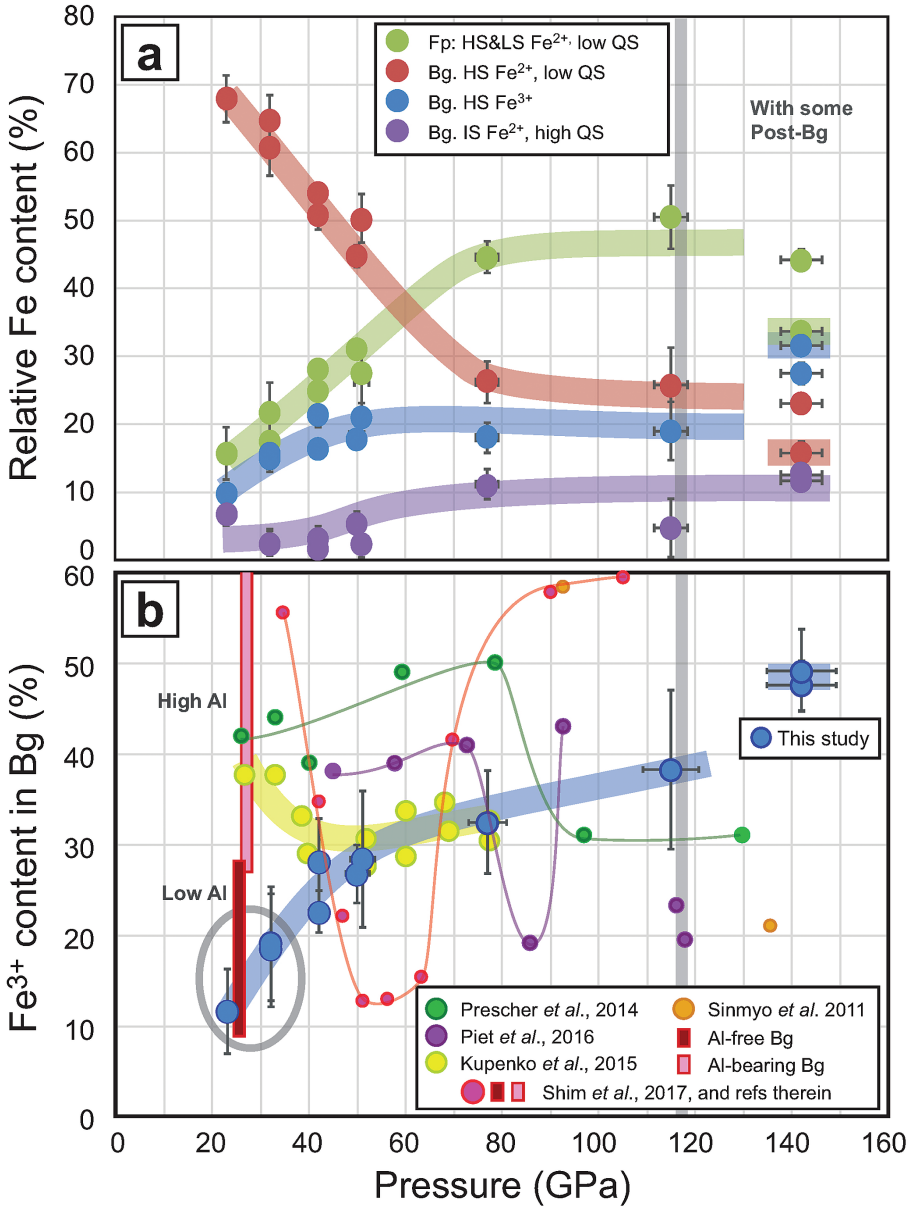

Figure 3 The mantle #Fe^{3+} refined from SMS measurements. **(a)** Major Fe contributions found in our sample are high spin and low spin Fe^{2+} in Fp (Kantor *et al.*, 2009) (both added to each other, green dots), high spin Fe^{2+} with low QS (red), intermediate spin Fe^{2+} (purple) and high spin Fe^{3+} (blue) in Bg (Kupenko *et al.*, 2015). Above ~40 GPa, corresponding to mantle depths greater than ~1000 km, the #Fe^{3+} in the bulk sample is almost constant at ~20 %. In the pressure field of post-Bg (~142 GPa), we performed two syntheses at ~2500 K (dot with a coloured trend superimposed) and ~3500 K. **(b)** When focusing on Bg properties, we observe a continuous increase of its #Fe^{3+} with pressure. At low pressure, our two samples plot in the field of previous Al-free (low Al) Bg compounds (see Shim *et al.*, 2017 and references therein). It could be associated with the remaining presence of Al-bearing garnet in our samples. On the other hand, Kupenko *et al.* (2015) found higher #Fe^{3+} in Bg in this pressure range (yellow dots). Above ~40 GPa, our data set produces a smooth trend which lies between the previous findings (Sinmyo *et al.*, 2011; Prescher *et al.*, 2014; Kupenko *et al.*, 2015; Piet *et al.*, 2016; Shim *et al.*, 2017).

Based on these assumptions, we calculate that 1/4 of the total amount of Fe^{3+} stored in the lower mantle Bg phase (with average #Fe^{3+} of 20 %) was not counterbalanced by the presence of Fe^0 after core segregation was completed. It corresponds to an O_2 excess of more than ~2.5 x 10^{22} mol O_2, compared to the current predominantly Fe^{2+}-bearing bulk mantle. This oxygen excess represents 500 to 1000 times the O_2 content in the Earth's atmosphere today.

Geodynamical Changes at the APT Possibly Produced the GOE

The fate of such a large oxygen excess (coupled to Fe^{3+} in Bg) trapped in the primordial lower mantle is a major question. It might have reached the Earth's surface (crust plus atmosphere) through volcanism. Analyses of Archean magma and mantle residues suggest that mantle sources have retained a constant, relatively oxidised, redox state for the last 3.5 Gyr or more (Delano, 2001; Canil, 2002). It is paradoxical that while early volcanic eruptions should have favoured an Earth's atmosphere dominated by oxidised volatile species (H_2O, CO_2, O_2), the Archean atmosphere remained anoxic (Shaw, 2008). This suggests a limited and/or inefficient mantle degassing during the Archean.

The tectonic regime prevailing during the Archean was dominated by microplates floating at the Earth's surface with a limited amount of subducted material (Condie and Kröner, 2013; Kamber, 2015). In such a regime, the lower mantle

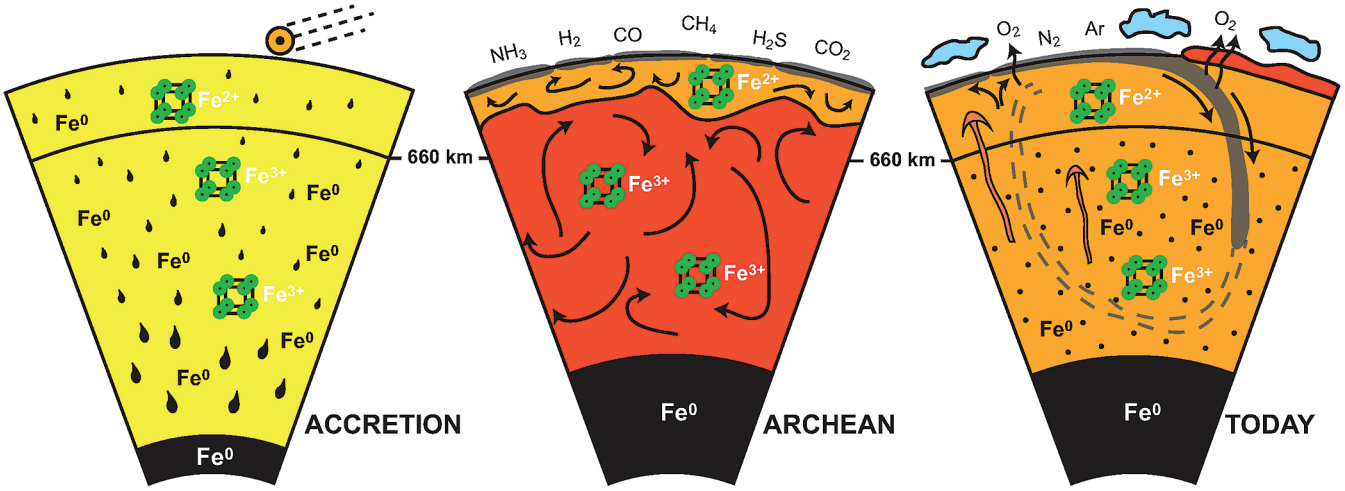

Figure 4 Change in the redox state of the deep mantle. During the Earth's accretion **(left)**, the descending iron droplets equilibrated chemically in a partially molten mantle, which contained a major amount of Bg below the 660 km discontinuity. After loss of the Fe^0, the lower mantle was left with a #Fe^{3+} of ~20 % (Fig. 3a). During the Archean **(centre)**, the oxidised deep mantle remained relatively isolated from the Earth's surface with a tectonic regime characterised by almost no subduction. At that time, the atmosphere was anoxic. The progressive transition to modern plate tectonics around the Archean to Proterozoic Transition greatly enhanced mantle mixing **(right)**. Subduction became the dominant mechanism, which associated to global mantle convection brought deeper material and then fresh lavas to the Earth's surface. Large amounts of oxygen were potentially degassed, due to the increase in volcanic fluxes and other sub-surface exchange processes. In this scheme, "Fe^{2+}" and "Fe^{3+}" indicate mantle fractions where the $Fe^{3+}/\Sigma Fe$ ratios are 2–3 % and ~20 %, respectively. Yellow, orange and red colours indicate the Earth's envelopes of Oxygen/ΣCations ratios that are lower (due to a Fe^0 excess), similar and higher (due to a Fe^{3+} excess), respectively, than the current mantle value.

material could have remained relatively isolated from shallow mantle processes, with only sporadic volcanism associated to deep mantle sources. Another argument in favour of a deep mantle which remained isolated for a long period of time is the relatively constant Lu/Hf ratio reported in rising plumes, suggesting that continents grew from nearly primordial unfractionated material (Guitreau *et al.*, 2012).

Around the APT, the early no subduction regime was progressively replaced by a modern style subduction regime (Fig. 4). This evolution could have been fairly chaotic, because episodic subductions have been identified during the late Archean (van Hunen and Moyen, 2012). Nevertheless, the transition resulted in major ultramafic volcanic events, greatly increasing the amount of fresh lava rising to the Earth's surface (Arndt and Davaille, 2013). We can estimate the flux of lower mantle material carried up by convection by assuming that it was equivalent to the slab volume subducting into the deep mantle today (Wen and Anderson, 1995). An upwelling flux of ~2.5 x 10^{11} m^3/year of primitive, oxidised, lower mantle material would correspond to the rise in excess of oxygen of ~1.5 x 10^{13} mol/year of O_2. With such a flux, it would take ~2.5 x 10^6 years for the ascent of an amount of oxygen "equivalent" to the current oxygen content of the Earth's atmosphere (Shaw, 2008).

Oscillations and overshoots in atmospheric oxygen pressure have been reported for a few 100 Myr around the APT (Bekker and Holland, 2012). They could be related to the chaotic transition between the two tectonic regimes, which might have resulted in an irregular rate of mantle mixing. In addition, the geological processes that could have accommodated the transfer of oxygen from a deep mantle source to the Earth's surface are multiple and complex. Partial melting is obviously a major component, because Fe^{3+} is an incompatible element. Fluids might also have played a role, because the nature of molecular components changes with the redox state (Gaillard *et al.*, 2011). At the time of the GOE, the increased fO_2 at the Earth's surface led to the precipitation of a large variety of minerals containing more oxidised ionic species, including carbonates, phosphates, sulphates, *etc.* (Sverjensky and Lee, 2010). Consequently, the amount of oxygen needed to induce the GOE must have far exceeded the current oxygen content of the Earth's atmosphere. The massive amount of oxygen that can be stored in Fe^{3+}-bearing Bg appears to be a unique redox source which can meet these requirements.

Acknowledgements

We warmly thank N. Bolfan-Casanova, P. Bonnand, J.-L. Devidal, M. Guitreau, I. Kupenko, H. Martin, G. Manthilake, M. Murakami, C. Prescher, A. Rosa, F. van Wyk de Vries, two anonymous reviewers and the editor W.L. Mao, for help and fruitful discussions. This work has been supported by the ANR contract "OxyDeep". This research was financed by ANR OxyDeep. This is Laboratory of Excellence ClerVolc contribution number 280.

Editor: Wendy Mao

Author Contributions

GP and DA prepared the DACs. MM, IK, DA, GP, SP performed XANES measurements, which were subsequently treated by MM. VC, DA, GP, AC, RR performed SMS measurements, which were subsequently treated by DA. DA and MM wrote the manuscript. All authors participated to discussions.

Additional Information

Supplementary Information accompanies this letter at www.geochemicalperspectivesletters.org/article1801.

Cite this letter as: Andrault, D., Muñoz, M., Pesce, G., Cerantola, V., Chumakov, A., Kantor, I., Pascarelli, S., Rüffer, R., Hennet, L. (2018) Large oxygen excess in the primitive mantle could be the source of the Great Oxygenation Event. *Geochem. Persp. Let.* 6, 5–10.

References

Abe, Y. (1997) Thermal and chemical evolution of the terrestrial magma ocean. *Physics of the Earth and Planetary Interiors* 100, 27–39.

Arndt, N., Davaille, A. (2013) Episodic Earth evolution. *Tectonophysics* 609, 661–674.

Badro, J., Rueff, J.P., Vanko, G., Monaco, G., Fiquet, G., Guyot, F. (2004) Electronic transitions in perovskite: possible nonconvecting layers in the lower mantle. *Science* 305, 383–386.

Bekker, A., Holland, H.D. (2012) Oxygen overshoot and recovery during the early Paleoproterozoic. *Earth and Planetary Science Letters* 317, 295–304.

Boujibar, A., Bolfan-Casanova, N., Andrault, D., Bouhifd, M.A., Trcera, N. (2016) Incorporation of Fe2+ and Fe3+ in bridgmanite during magma ocean crystallization. *American Mineralogist* 101, 1560–1570.

Buick, R. (2008) When did oxygenic photosynthesis evolve? *Philosophical Transactions of the Royal Society B-Biological Sciences* 363, 2731–2743.

Canil, D. (2002) Vanadium in peridotites, mantle redox and tectonic environments: Archean to present. *Earth and Planetary Science Letters* 195, 75–90.

Condie, K.C., Kröner, A. (2013) The building blocks of continental crust: Evidence for a major change in the tectonic setting of continental growth at the end of the Archean. *Gondwana Research* 23, 394–402.

Delano, J.W. (2001) Redox history of the Earth's interior since similar to 3900 Ma: Implications for prebiotic molecules. *Origins of Life and Evolution of the Biosphere* 31, 311–341.

Frost, D.J., Liebske, C., Langenhorst, F., McCammon, C.A., Tronnes, R.G., Rubie, D.C. (2004) Experimental evidence for the existence of iron-rich metal in the Earth's lower mantle. *Nature* 428, 409–412.

Frost, D.J., Mann, U., Asahara, Y., Rubie, D.C. (2008) The redox state of the mantle during and just after core formation. *Philosophical Transactions of the Royal Society A-Mathematical Physical and Engineering Sciences* 366, 4315–4337.

Gaillard, F., Scaillet, B., Arndt, N.T. (2011) Atmospheric oxygenation caused by a change in volcanic degassing pressure. *Nature* 478, 229–232.

Guitreau, M., Blichert-Toft, J., Martin, H., Mojzsis, S.J., Albarede, F. (2012) Hafnium isotope evidence from Archean granitic rocks for deep-mantle origin of continental crust. *Earth and Planetary Science Letters* 337, 211–223.

Irifune, T., Koizumi, T., Ando, J. (1996) An experimental study of the garnet-perovskite transformation in the system MgSiO3-Mg3Al2Si3O12. *Physics of the Earth and Planetary Interiors* 96, 147–157.

Kamber, B.S. (2015) The evolving nature of terrestrial crust from the Hadean, through the Archaean, into the Proterozoic. *Precambrian Research* 258, 48–82.

Kantor, I., Dubrovinsky, L., McCammon, C., Steinle-Neumann, G., Kantor, A., Skorodumova, N., Pascarelli, S., Aquilanti, G. (2009) Short-range order and Fe clustering in Mg1-xFexO under high pressure. *Physical Review B* 80, 014204.

Kupenko, I., McCammon, C., Sinmyo, R., Cerantola, V., Potapkin, V., Chumakov, A.I., Kantor, A., Ruffer, R., Dubrovinsky, L. (2015) Oxidation state of the lower mantle: In situ observations of the iron electronic configuration in bridgmanite at extreme conditions. *Earth and Planetary Science Letters* 423, 78–86.

Piet, H., Badro, J., Nabiei, F., Dennenwaldt, T., Shim, S.H., Cantoni, M., Hebert, C., Gillet, P. (2016) Spin and valence dependence of iron partitioning in Earth's deep mantle. *Proceedings of the National Academy of Sciences of the United States of America* 113, 11127–11130.

Prescher, C., Langenhorst, F., Dubrovinsky, L.S., Prakapenka, V.B., Miyajima, N. (2014) The effect of Fe spin crossovers on its partitioning behavior and oxidation state in a pyrolitic Earth's lower mantle system. *Earth and Planetary Science Letters* 399, 86–91.

Shaw, G.H. (2008) Earth's atmosphere - Hadean to early Proterozoic. *Chemie Der Erde-Geochemistry* 68, 235–264.

Shim, S.-H., Grocholski, B., Ye, Y., Alp, E.E., Xu, S., Morgan, D., Meng, Y., Prakapenka, V.B. (2017) Stability of ferrous-iron-rich bridgmanite under reducing midmantle conditions. *Proceedings of the National Academy of Sciences of the United States of America* 114, 6468–6473.

Sinmyo, R., Hirose, K., Muto, S., Ohishi, Y., Akira, Y. (2011) The valence state and partitioning of iron in the Earth's lowermost mantle. *Journal of Geophysical Research* 116, B07205.

Sverjensky, D.A., Lee, N. (2010) The Great Oxidation Event and Mineral Diversification. *Elements* 6, 31–36.

van Hunen, J., Moyen, J.-F. (2012) Archean Subduction: Fact or Fiction? *Annual Review of Earth and Planetary Sciences* 40, 195–219.

Wen, L.X., Anderson, D.L. (1995) The fate of slabs inferred from seismic tomography and 130 million years of subduction. *Earth and Planetary Science Letters* 133, 185–198.

Wilke, M., Farges, F., Petit, P.E., Brown, J.G.E., Martin, F. (2001) Oxidation state and coordination of Fe in minerals: An Fe K-XANES spectroscopic study. *American Mineralogist* 86, 714–730.

Yoshino, T., Walter, M.J., Katsura, T. (2003) Core formation in planetesimals triggered by permeable flow. *Nature* 422, 154–157.

Geochemical Perspectives Letters

Large oxygen excess in the primitive mantle could be the source of the Great Oxygenation Event

D. Andrault, M. Muñoz, G. Pesce, V. Cerantola, A. Chumakov, I. Kantor, S. Pascarelli, R. Rüffer, L. Hennet

Supplementary Information

The Supplementary Information includes:

- Methods
- Table S-1 to S-3
- Figures S-1 to S-8
- Supplementary Information References

Methods

We probed the Fe behaviour in various mineral assemblages at pressure and temperature conditions typical of the lower mantle using X-ray absorption near edge spectroscopy (XANES) and synchrotron Mossbauer spectroscopy (SMS).

1. Starting materials

We used different types of starting material (Table S-1): (i) ferropericlase ($Mg_{0.8}Fe_{0.2}O$), (ii) a fine powder mixture of a natural enstatite with Fe/(Mg+Fe) = 0.17 mixed with Al_2O_3 to produce an Fe/Al ratio of 1 ($Al_{0.17}$-$Mg_{0.83}Fe_{0.17}SiO_3$), and (iii) three synthetic glasses with compositions typical of a chondritic mantle with two times more Fe, to improve the XANES signal; with ^{57}Fe, to improve the SMS signal; and without Al. For our chondritic-type composition (the sample probed by SMS, for example), we expect a mineral mixture composed of 75.3 %, 17.0 %, 7.7 % of Bg, Fp and $CaSiO_3$ perovskite (CaPv), respectively. The typical atomic Fe/(Mg+Fe) ratio is ~0.11. Glasses were prepared using the high temperature aerodynamic levitation technique associated with CO_2 laser heating (Hennet *et al.*, 2011). The gas mixture (Ar with less than 0.05 ppm of oxygen) was adjusted in order to obtain no metal Fe and a minimum of Fe^{3+}. We determined the $Fe^{3+}/\Sigma Fe$ ratio (#Fe^{3+}) as 7-8 %, using Mossbauer spectroscopy (see below, Fig. S-5). For all compositions, powders were ground for several minutes in a glove bag with a flow of nitrogen just before loading the pressure chamber, in order to prevent water contamination.

2. Experimental methods

We used the membrane-type diamond anvil cell (DAC) mounted with diamonds with beveled culets with diameters from 250/300 to 75/300 µm, depending on the target pressure. Pre-indented Re-gaskets were drilled in the centre using a pulsed laser to a diameter of ~1/3 of the internal culet diameter. Pressures at 300 K were determined from the Raman-shift of the major peak of the diamond surface in contact with the sample. The sample pressure can increase during the laser heating (*e.g.*, ~5 GPa for heating to 2500 K) due to the effect of thermal pressure (Andrault *et al.*, 1998). Up to ~60 GPa, we sometimes used a thin layer of KCl between the sample and diamonds to minimise the axial temperature gradient within the sample. At higher pressures, we used no pressure medium, because the use of a KCl layer resulted in a significant deterioration of the XANES and SMS spectra. For XANES measurements, thin diamond anvils 1.6 mm in height were selected in order to reduce the X-ray absorption at the Fe K-edge energy (7112 eV). Also, we added a piece of KCl on the sample side in the gasket hole to allow measurement of the X-ray beam intensity

(I_0).

A similar strategy was used on both ID24 and ID18 beamlines for the laser heating. After the target pressure was achieved, we transformed the samples using two fibre lasers of 100 W, with available on-line systems (Kupenko *et al.*, 2012). For final laser alignments, we used optical lenses with focal lengths of 35 or 50 mm. We defocused lasers until the size of the hot spot on the sample was 10-15 μm. The sample temperature was monitored by thermal radiometry, and was progressively increased up to 2000, 2500 or 3500 K (Table S-2). At each pressure investigated, we slowly scanned the sample between the two lasers to anneal the whole sample volume, for about 30 minutes, before the lasers were quenched. For SMS measurements, we used one fresh sample per pressure condition. This procedure prevents potential problems associated with slow atomic diffusion between grains, once the starting material has already been transformed. For XANES measurements, each sample was recompressed and reheated to the maximum temperature over a pressure range of 30-40 GPa, before another sample was synthesised at a different pressure range (Table S-2). Some chemical segregation could occur during the scan of the laser spot on the sample. Increasing the Fp and Bg grain size might produce heterogeneities at the level of microns (Fig. 1). However, X-ray beams were significantly larger than the grain size, with FWHM of 5 μm and 10-15 μm in case of XANES and SMS, respectively. For XANES, we recorded maps on which measurements were averaged.

3. XANES results

3.1 Experimental methods. XANES hyperspectral mapping was performed at the Fe K-edge using dispersive spectroscopy at the ID24 beamline (ESRF) (Muñoz *et al.*, 2006). We used an Si(220) bent crystal polychromator that provides the best compromise between spectral resolution for pre-edge absorption peak analysis, X-ray flux and k-space extension. The polychromatic X-ray beam was focused to a ~5×5 μm² spot at the sample location. The absorption spectrum μ(E) is equal to $\ln(I_0/I_1)$ where I_1, and I_0, are X-ray intensities recorded by the spatially resolved CCD detector through the sample position, and a piece of KCl, respectively. Both I_0 and I_1 were measured through diamonds. The DAC was rotated in the X-ray beam to remove diffraction peaks of diamonds from the energy range of interest. Acquisition time was a few minutes. To improve statistics and prevent potential artefacts related to grain growth and sample heterogeneity, we performed sample maps in the diamond anvil cell with a spatial resolution of ~5x5 μm², on which the recorded XANES signals were averaged (Munoz *et al.*, 2008).

The basic methodology was similar to our previous work (Andrault *et al.*, 2010). However, the quality of measurements was much improved to the point that we could use the pre-edge features located around 7110-7115 eV (Fig. S-2) to refine the $Fe^{3+}/(Fe^{2+}+Fe^{3+})$ ratio (#Fe^{3+}) in our samples *in situ* at high pressures. Fit to experimental pre-edge was performed between 7108 and 7118 eV using 3 pseudo-voigt peak-components with a fixed band width of 2 eV and a 50:50 Lorentz/Gaussian peak shape (Fig. S-4). The pre-edge centroid energy (PCE) was then calculated by summing each peak position weighted by its corresponding area fraction (Wilke *et al.*, 2001; Munoz *et al.*, 2013). The energy calibration requires the use of internal standards. In our study, we used olivine as a standard for the PCE, to match the value of (Wilke *et al.*, 2001). Also, in order to compare our results with previous PCE values reported for Bg (Boujibar *et al.*, 2016), we corrected their PCE value using their "internally consistent" siderite reference. In this way, all our PCE values are consistent with each other.

3.2 Fe partitioning between Bg and Fp. We first investigated the evolution of XANES features for two reference compounds, Fp ($Mg_{0.8}Fe_{0.2}O$) and Bg ($Al_{0.17}$-$Mg_{0.83}Fe_{0.17}SiO_3$), upon compression to 104 GPa and 62 GPa, respectively (Fig. S-1). For Bg, we performed laser annealing to ~2500 K for several minutes after each pressure increment, to enable a potential evolution of the point-defect population (e.g., Fe^{3+} and oxygen vacancies) in the Bg lattice. The pressure evolution of XANES features is very compatible with previous work (Narygina *et al.*, 2009). The two reference compounds present well contrasted XANES shapes. Fp shows a well-structured XANES with several maxima and minima in the energy domain of ~90 eV available in this study. The energy position of the first peak at 7120-7125 eV is found to be independent of pressure, while other contributions shift to higher energies with increasing pressure (corresponding to a decrease in interatomic distance). The spin transition reported for Fe in Fp in the pressure range investigated (Badro *et al.*, 2003) does not produce any significant effect on XANES features. In contrast, the XANES shape of Bg is rounded and only mildly affected by pressure, at least up to 62 GPa. The difference in shape and pressure evolution of Bg and Fp XANES results facilitate the spectral deconvolution in our samples composed of a mixture of both phases (Munoz *et al.*, 2008; Narygina *et al.*, 2011).

We then investigated our two synthetic glasses with compositions typical to chondritic mantle, but with either two times more Fe or without Al (Tables S-1 and S-2). At each P-T condition, the spectral deconvolution was performed using a linear combination of XANES spectra of Fp and Bg recorded at a similar pressure (Fig. S-2) (Munoz *et al.*, 2008; Andrault *et al.*, 2010). It provides fractions of Fe located in Fp and Bg phases as a function of the experimental pressure and temperature. It yields the Fe partition coefficient between Bg and Fp ($K_{Fe}^{Bg/Fp} = X_{Fe}^{Bg} X_{Mg}^{Fp} / X_{Mg}^{Bg} X_{Fe}^{Fp}$), based on the molar ratio of Fp and Bg expected for each starting material. At low pressure, we observe significantly different $K_{Fe}^{Bg/Fp}$ for both samples, probably because they contain different amounts of Al and Fe (Fig. S-3). This effect has been systematically studied in the past at moderate pressures (Wood and Rubie, 1996). In contrast, the refined $K_{Fe}^{Bg/Fp}$ values plot close to each other for all samples above ~50 GPa. Overall, we observe a large decrease in $K_{Fe}^{Bg/Fp}$ with increasing pressure, which could be related to the change in spin of Fe in Fp (Badro *et al.*, 2004; Lin *et al.*, 2007). Our results suggest ~5 (+/- 1) times more Fe in Fp, compared to Bg, in the lower mantle for depths greater than ~1250 km.

3.3 Fe redox state. The PCEs of $(Mg_{0.8}Fe_{0.2})O$ Fp and $Al_{0.17}$-$(Mg_{0.83}Fe_{0.17}SiO_3)$ Bg references plot within the range of energy values typical of many Fe^{2+}-Fe^{3+} minerals (Wilke *et al.*, 2001) (Fig. 2). Our $Mg_{0.9}Fe_{0.1}O$ reference Fp contains almost exclusively Fe^{2+}. However, its PCE still plots at relatively high energy, in agreement with previous reports (Wilke *et al.*, 2001). Concerning our Bg reference compound, we performed an SMS analysis on the recovered sample and refined an $\#Fe^{3+}$ of 27(3) % (Fig. S-6).

With increasing pressure, PCEs of both Fp and Bg increase by 0.3-0.4 eV up to ~30 GPa, before they progressively decrease at higher pressure. The situation is complicated, however, because we lack knowledge about the pressure effect on the energy position and intensity of pre-edge features. At this stage, this means that our XANES measurements for the determination of the redox state in our samples remain qualitative. Still, we observe that Bg plots (i) at relatively higher energies, compared to Fp, most likely due to a higher Fe^{3+}-content in Bg (McCammon, 1997), and (ii) 2 to 3 times higher for integrated areas. The relatively high intensities are likely due to a less centrosymmetric site in Bg (the Fe-O_{12} dodecahedral site is highly distorted), compared to the Fe-O_6 octahedral site in Fp. Accordingly, when Fp and Bg coexist in a same sample, the Fe fraction located in the Bg should dominate the pre-edge features.

Both Fp and Bg reference compounds show a significant decrease in PCE with increasing the pressure (Fig. 2). This effect cannot be related to a change in $\#Fe^{3+}$ in Fp, because the sample was compressed at 300 K. Explanations for this pressure effect could be complex, because pre-edge features are related to intrinsic 1s-3d electronic transitions in Fe. For Bg, the pressure evolution is found to be parallel to that of Fp, suggesting a constant Fe^{3+}-content in the pressure range investigated, despite the laser annealing performed after each increment of pressure increase from 35 to 62 GPa.

For our two chondritic-type samples containing both Bg and Fp, PCEs are found at similar, or slightly higher, energies than observed for the Bg reference. One possible explanation for this is major partitioning of Fe^{2+} to Fp (Prescher *et al.*, 2014), which leaves Bg with a higher $\#Fe^{3+}$. Because Bg presents significantly more intense pre-edge features than Fp (Wilke *et al.*, 2001), it yields a higher PCE for the bulk sample. We also observe a global increase in the centroid energy with increasing pressure (Fig. 2). This observation contrasts with trends observed for the reference compounds, Fp and Bg, which excludes a decrease in the bulk $\#Fe^{3+}$ with increasing pressure in our chondritic-type samples.

4. SMS results

4.1 Experimental methods. SMS was performed with the Nuclear Resonance ID18 beamline (ESRF) using the (111) Bragg reflection of a $^{57}FeBO_3$ single crystal mounted on a Wissel velocity transducer driven with a sinusoidal wave form (Potapkin *et al.*, 2012). The crystal temperature was adjusted to achieve a maximum X-ray flux for an energy resolution of ~6 neV. Energy was tuneable over a range of about ± 0.6 μeV. The X-ray beam was focused to 15 x 10 μm^2 using two Kirkpatrick-Baez multilayer optics. The linewidth of the SMS and the absolute position of the center-shift (CS) was controlled before and after each measurement using a $K_2Mg^{57}Fe(CN)_6$ reference single line absorber. The velocity scale was calibrated using 25 μm thick natural α-Fe foil. The average collection time was 4 to 10 hours for samples located inside the DAC.

A new sample was used at each experimental pressure. We recorded 8 SMS spectra of the glass upon compression to 123 GPa and several SMS spectra on 8 different samples transformed at high temperatures at pressures up to 142 GPa. The complete sample transformation was monitored based on (i) our knowledge of the minimum time required at 2500 K for the phase transformation (Andrault *et al.*, 2010) and (ii) the change with heating time of SMS features. For example, the main absorption peak of the compressed glass and the transformed sample plot around -0.5 mm/s or + 0.5 mm/s, respectively, at high pressures. At lower pressures, an intense contribution at a relative velocity position of 2-2.5 mm/s is present in the starting glass and not in the transformed sample (Fig. S-5). All SMS spectra which showed a mixture of the starting glass and transformed material were discarded.

All spectra were fitted using a full transmission integral with a normalized Lorentzian-squared source line-shape using the MossA software package (Prescher *et al.*, 2012). Previous articles have already investigated the typical Fe SMS signal in pure Bg (Kupenko *et al.*, 2014) and pure Fp (Kantor *et al.*, 2009) under pressure. For both phases, the central shift (CS) and the quadrupole splitting (QS) of various Fe atomic sites were reported as a function of pressure up ~80 GPa. We have relied strongly on these previous studies to deconvolve our SMS patterns recorded for equilibrated mixtures of Bg (or Post-Bg) and Fp.

4.2 Spin transition in Fp. All our SMS patterns could be fitted by a sum of 5 different Fe contributions: high-spin Fe^{2+} and low-spin Fe^{2+} in Fp (Kantor *et al.*, 2009), high-spin Fe^{2+} with low-QS, intermediate-spin Fe^{2+} and high-spin Fe^{3+} in Bg (McCammon *et al.*, 2008; Kupenko *et al.*, 2014) (Fig. S-7). Due to a large number of parameters, we first adjusted the fraction of each Fe contribution fixing all CS and QS values to those reported in the literature. We then optimised the CS and QS values. The first observation is a clear change in both CS and QS for Fe^{2+} in Fp, at between 51 and 77 GPa (Fig. S-8), associated with the progressive HS to LS transition of the Fe in Fp at high temperature (Lin *et al.*, 2007). This transition pressure is compatible with a FeO/(MgO+FeO) ratio between 0.2 and 0.5 (Fei *et al.*, 2007). It is compatible with an FeO-content in Fp of 25-30 %, which we can estimate based on the relative intensity between the different Fe components present in the SMS spectrum of the sample synthesized at ~77 GPa (see below for the method to calculate this FeO-content). All other CS and QS parameters follow a smooth evolution with pressure which is compatible with previous works (Kantor *et al.*, 2009; Kupenko *et al.*, 2014). In particular, SMS patterns fit well with two

Fe^{2+} contributions in Bg, HS and IS, with a significant amount of IS Fe^{2+} above ~30 GPa.

One could argue that artefacts arise in our study, due to the fact that we neglected a potential $Fe^{3\#}$ for Fp. However, such an Fe-contribution is not observed in our SMS patterns. In addition, although it is reported in one EELS study that uses the most oxidised starting material (Prescher *et al.*, 2014), it is not observed in the other one (Piet *et al.*, 2016), nor in another report using EELS on quenched large volume press samples (Irifune *et al.*, 2010).

4.3 Fe-partitioning between Fp and Bg. We observe a progressive increase in Fe^{2+}-content in Fp (combining HS and LS contributions) up to a pressure of ~80 GPa (Fig. 3b) which is related to the spin transition described above. At an experimental pressure of ~50 GPa, for example, the sum of Fe contributions in Bg and Fp indicates that 70 % of the Fe is located in Bg and 30 % in Fp (Fig. 3a). Due to the starting material composition (75.3 % Bg and 17.0 % Fp, Table S-1), it yields a $K_{Fe}^{Bg/Fp}$ of ~0.5. This value, as well as other $K_{Fe}^{Bg/Fp}$ values calculated in the same way based on all our SMS results, are in good agreement with our XANES results (Fig. S-3). In the pressure field where post-Bg becomes a major component, we calculate a $K_{Fe}^{Bg/Fp}$ of ~0.39(3) and ~0.22(3) for sample synthesis at ~2500 K and ~3500 K, respectively. The higher K_D value measured at 142 GPa, relative to that at lower pressures, suggests that Fe is less incompatible in post-Bg, in agreement with previous work (Murakami *et al.*, 2005).

4.4 Fe redox state. At pressures below 30-35 GPa, we found a bulk $\#Fe^{3+}$ of ~10-15 % (Fig. 3a), which fits well with the high-spin Fe^{3+} contribution in Bg (Fig. S-7). This $\#Fe^{3+}$ is comparable to the 15 % (McCammon *et al.*, 2008) and 21 % (Boujibar *et al.*, 2016) given for the Bg lattice, but it plots significantly lower than other values of $\#Fe^{3+}$ for Bg of up to 30 % or even 42 % in pyrolitic samples (McCammon *et al.*, 2008). Our data set also plot significantly lower than a previous study performed using the same experimental tools on a single phase of Bg pre-synthesized using the large volume press (LVP) (Kupenko *et al.*, 2015). Al-bearing garnets are stable below 30-35 GPa (e.g. (Irifune et al., 1996)). Their potential presence in our low-pressure samples would significantly decrease the Al-content in Bg and would in turn decrease its $\#Fe^{3+}$ (Fig. 3b). In our LH-DAC experiments, we do not have high enough resolution to further constraint the mantle $\#Fe^{3+}$ between 24 and 30-35 GPa, compared to previous LVP works. Nevertheless, it is clear that one should expect (i) a relatively low $\#Fe^{3+}$ in Bg (typically 10 to 25 %) in the presence of garnet and (ii) a higher $\#Fe^{3+}$ in Bg ($\#Fe^{3+}$ of 25-30%, (Kupenko *et al.*, 2015)) in the absence of garnet. We note that the uncertainty concerning the mantle $\#Fe^{3+}$ between 24 and 30-35 GPa does not have a significant impact on the main conclusions of our work.

In the pressure range between ~40 and 115 GPa, the bulk $\#Fe^{3+}$ remains relatively constant at ~20 % (Fig. 3a). Due to a progressive decrease in Fe^{2+}-content in Bg, the $\#Fe^{3+}$ in Bg increases from ~25 % to ~35 % over this pressure range (Fig. 3b). Above 40 GPa, there is a very good agreement between our data set and the values presented by (Kupenko *et al.*, 2015), which were obtained using a very similar approach. In contrast, other previous data sets plot sometimes above, sometimes below our experimental trend. Differences in experimental conditions may explain the observed discrepancies: (i) A relatively high $\#Fe^{3+}$ was reported below ~80 GPa in some studies that used relatively oxidised starting materials ($\#Fe^{3+}$ of 25 % and 42 % in (Piet *et al.*, 2016) and (Prescher *et al.*, 2014), respectively), compared to the $\#Fe^{3+}$ of 7-8 % in our glass starting material. (ii) A relatively low $\#Fe^{3+}$ was measured in Bg samples synthesised between 50 and 70 GPa (Shim *et al.*, 2017). However, this is the pressure range where Fe^{2+} undergoes a change in spin in Fp, favoring the partitioning of Fe^{2+} to the Fp phase when Fp and Bg coexist at mantle-relevant compositions. In the absence of Fp, the Fe^{2+} remains in Bg leading to a relatively low $\#Fe^{3+}$. (iii) The very high $\#Fe^{3+}$ reported by (Sinmyo *et al.*, 2011) are difficult to explain. The great care put in to controlling the redox state of starting materials in this latter study may have been undermined by the use of gels, which can be high in water content.

In the pressure field where post-Bg becomes a major component, we measure a significantly higher bulk $\#Fe^{3+}$, 28 % to 32 %, compared to at lower pressure. This mantle $\#Fe^{3+}$ corresponds to an $\#Fe^{3+}$ of a mixture of Bg and post-Bg close to 50 % (Fig. 3).

Supplementary Tables

Table S-1 Composition of the starting material.

Sample Material	Fp-20 Synthetic	Al-En Powder-mix	CI-NoAl Glass	CI-2Fe Glass	CI-^{57}Fe Glass
SiO_2	-	48.82	50.10	44.87	50.46
TiO_2	-	-	0.21	0.19	0.05
Al_2O_3	-	14.08	0.00	3.73	4.14
Cr_2O_3	-	-	0.31	0.28	0.01
FeO	30.83	9.92	7.50	13.43	7.68
MgO	69.17	27.18	35.42	31.72	33.51
CaO	-	-	5.94	5.32	3.63
Na_2O	-	-	0.52	0.47	0.53
Al/Fe	0	1	0	0.39	0.76
Bg/(Bg+Fp)	0	1	0.72	0.67	0.82

En, Fp and Bg stand for enstatite, ferropericlase and bridgmanite, respectively. The expected Bg/(Bg+Fp) ratio is calculated including all Al_2O_3 in the Bg phase with the coupled substitution mechanism.

Table S-2 Summary of experimental runs.

Sample	Analyt. Tech.	P-range (GPa)	Strategy	Temperature (K)
Fp-20	XANES	15-104	A	300
Al-En	XANES	35-62	B	2500
CI-NoAl	XANES	33-66	B	2500
CI-2Fe	XANES	46-122	B	2500
CI-^{57}Fe	SMS	0-123	A	300
CI-^{57}Fe	SMS	23-142	C	2000 to 3500

Experimental conditions A, B, and C correspond to compression at 300 K, compression with laser annealing at each pressure step, and synthesis of a new sample at each pressure step, respectively.

Table S-3 List of the SMS parameters.

Press. GPa	Temp. K	Fp: Fe2+ HS and LS				Bg: Fe2+ HS and Low QS				Bg: Fe3+ HS				Bg: Fe2+ IS				Chi-square
		CS	QS	FWHM	Int.	CS	QS	FWHM	Int.	CS	QS	FWHM	Int.	CS	QS	FWHM	Int.	
23	2000	0.936	1.04	0.574	15.71	1.097	2.228	0.9	67.9	0.288	1.162	0.4	9.78	1.205	3.505	0.35	6.611	0.73
32	2000	0.889	1.15	0.509	17.5	1.042	2.269	0.795	64.74	0.36	1	0.4	15.17	1.1	3.6	0.35	2.585	1.062
32	2500	0.86	1.15	0.577	21.81	1.028	2.305	0.791	60.65	0.36	1	0.4	14.94	1.1	3.6	0.35	2.602	1.209
42	2500	0.866	1.14	0.42	27.64	1.079	2.211	0.848	54.22	0.36	1	0.4	16.38	1.05	3.7	0.35	1.762	1.105
42	3500	0.852	1.152	0.495	24.56	1.141	2.224	0.85	50.85	0.346	0.989	0.4	21.16	1.05	3.822	0.35	3.424	0.93
50	2500	0.824	0.936	0.45	31.08	1.039	2.029	0.903	44.77	0.241	1	0.4	18.47	1.05	3.8	0.35	5.678	1.8
51	2500	0.909	1.023	0.721	26.17	1.084	2.326	0.85	50.31	0.304	1.174	0.4	21	1.122	3.85	0.35	2.522	1.13
77	2500	0.436	0.278	0.45	44.61	1	2.2	0.903	26.19	0.166	1.2	0.4	18.02	0.982	4.003	0.35	11.19	0.58
115	2500	0.358	0.221	0.45	50.5	1	2.2	0.903	25.79	0.166	1.245	0.45	18.98	0.982	4	0.35	4.736	0.63
142	2500	0.326	0.25	0.5	33.68	1.045	2.5	0.434	23.05	0.131	1.471	0.5	31.59	0.98	4.15	0.35	11.68	1.425
142	3500	0.392	0.25	0.5	44.2	1.069	2.309	0.434	15.77	0.2	1.3	0.5	27.49	0.98	4.15	0.35	12.53	0.725

Abbreviations are for Pressure (Press.), Temperature (Temp.), High-Spin (HS), Low-spin (LS), Intermediate spin (IS), Central shift (CS), quadrupole splitting (QS), Full width half maximum (FWHM), Relative intensity (Int.). For Fp, we present the results for HS and LS Fe^{2+} in the same column.

Supplementary Figures

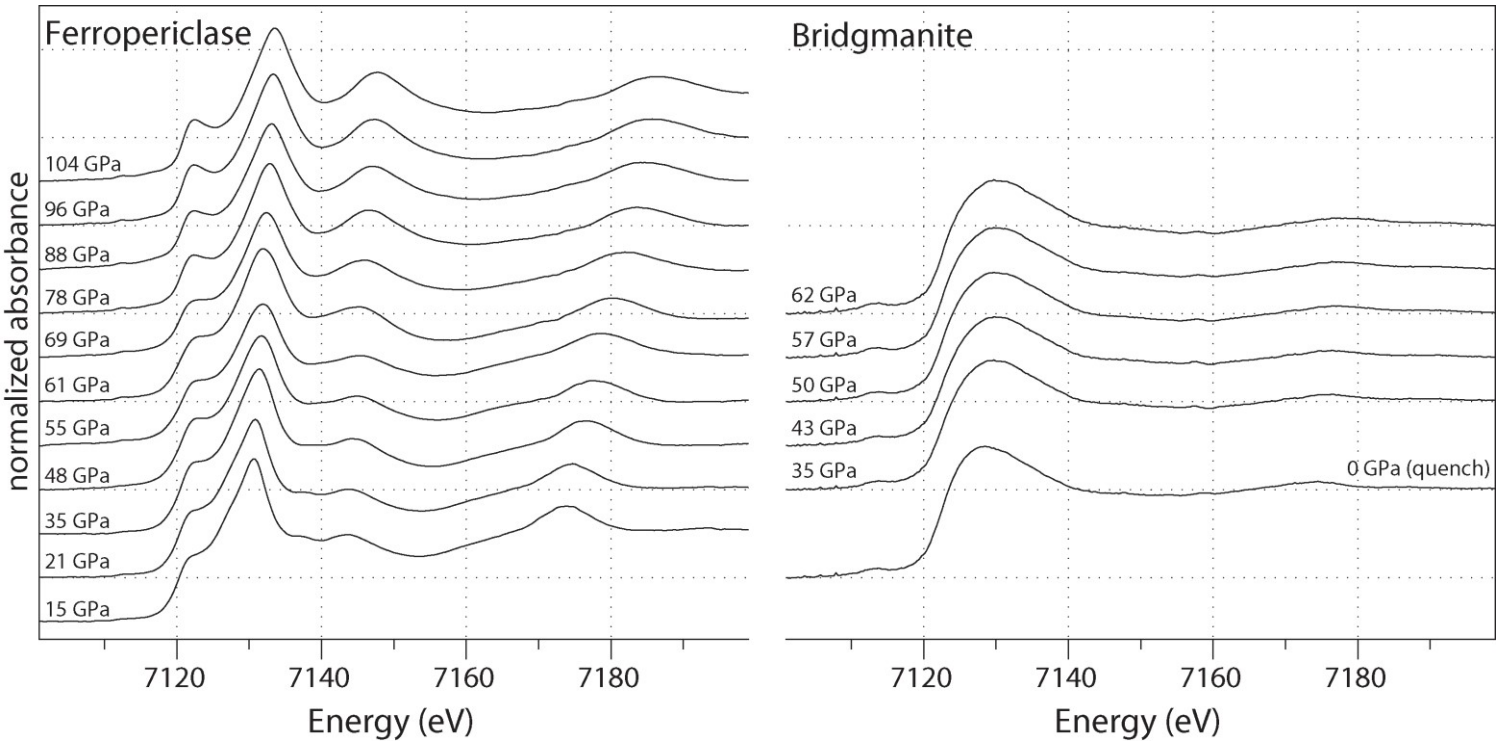

Figure S-1 XANES spectra of Fp and Bg standards upon compression to 104 and 62 GPa, respectively. Reference compounds consist in $Mg_{0.8}Fe_{0.2}O$ Fp **(left)** and $Al_{0.17}$-($Mg_{0.83}Fe_{0.17}SiO_3$) Bg **(right)**. The Fe K-edge absorption spectra are all normalised.

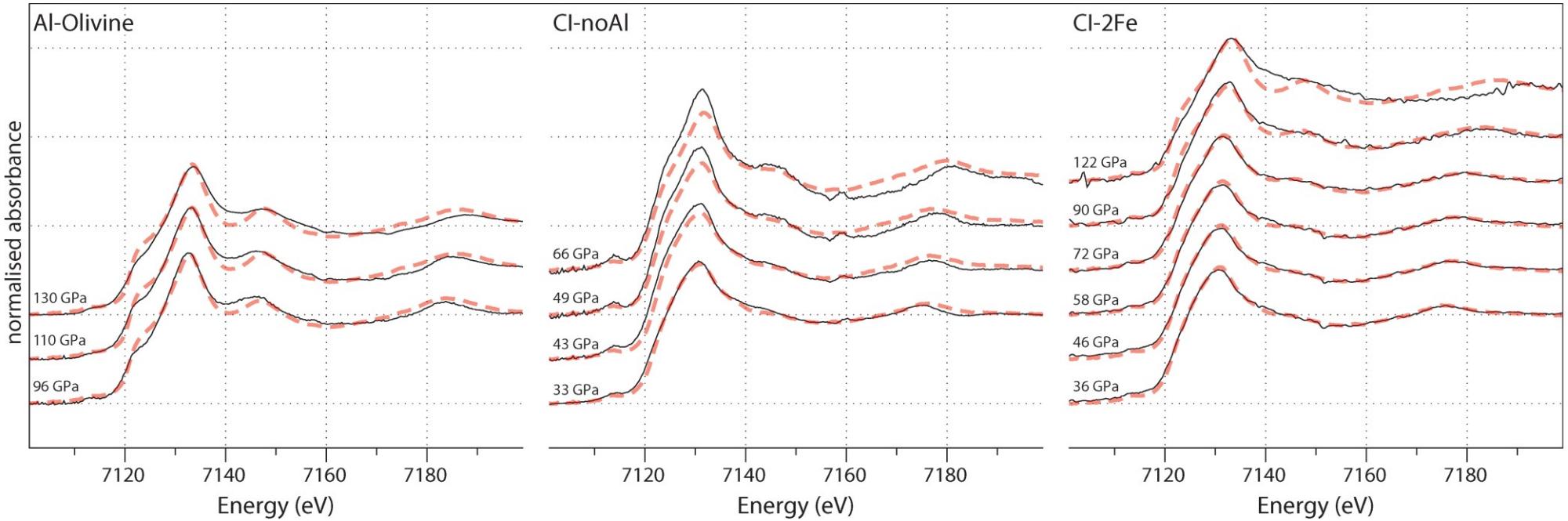

Figure S-2 Deconvolution of XANES spectra of our samples. Sample compositions are typical chondritic-type mantle, with no Al (CI-noAl, left) or two times more Fe (CI-2Fe, right) (see Tables S-1 and S-2). We report experimental spectra (black lines) together with their respective fits (red dashed lines) based on the linear combination of reference spectra (Fp and Bg, from Fig. S-1) taken at similar pressures. We used the pre-edge features located around 7110-7115 eV to qualitatively refine the $\#Fe^{3+}$ in our samples (see Fig. S-4).

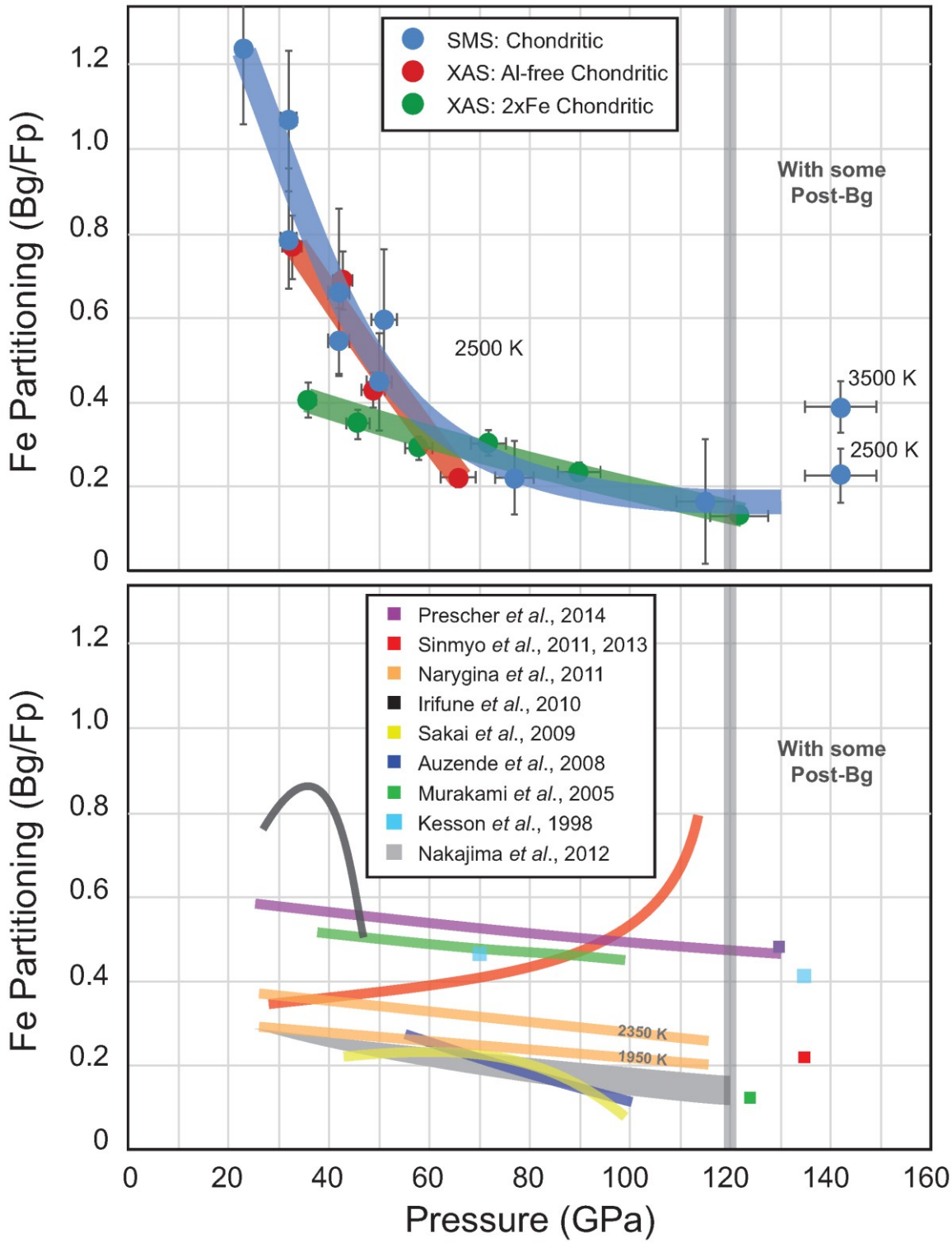

Figure S-3 Fe partition coefficient ($K_{Fe}^{Bg/Fp}$) between Bg and Fp. Our experimental data (top frame) show a large decrease of $K_{Fe}^{Bg/Fp}$ with increasing pressure up to the pressure of ~60 GPa, which can be explained by the spin transition of Fe in Fp (Lin *et al.*, 2007). Our data set plot in the same range as the several previous reports performed using various mantle-relevant compositions (bottom frame) (Kesson *et al.*, 1998; Murakami *et al.*, 2005; Auzende *et al.*, 2008; Sakai *et al.*, 2009; Irifune *et al.*, 2010; Narygina *et al.*, 2011; Sinmyo *et al.*, 2011; Nakajima *et al.*, 2012; Sinmyo and Hirose, 2013; Prescher *et al.*, 2014).

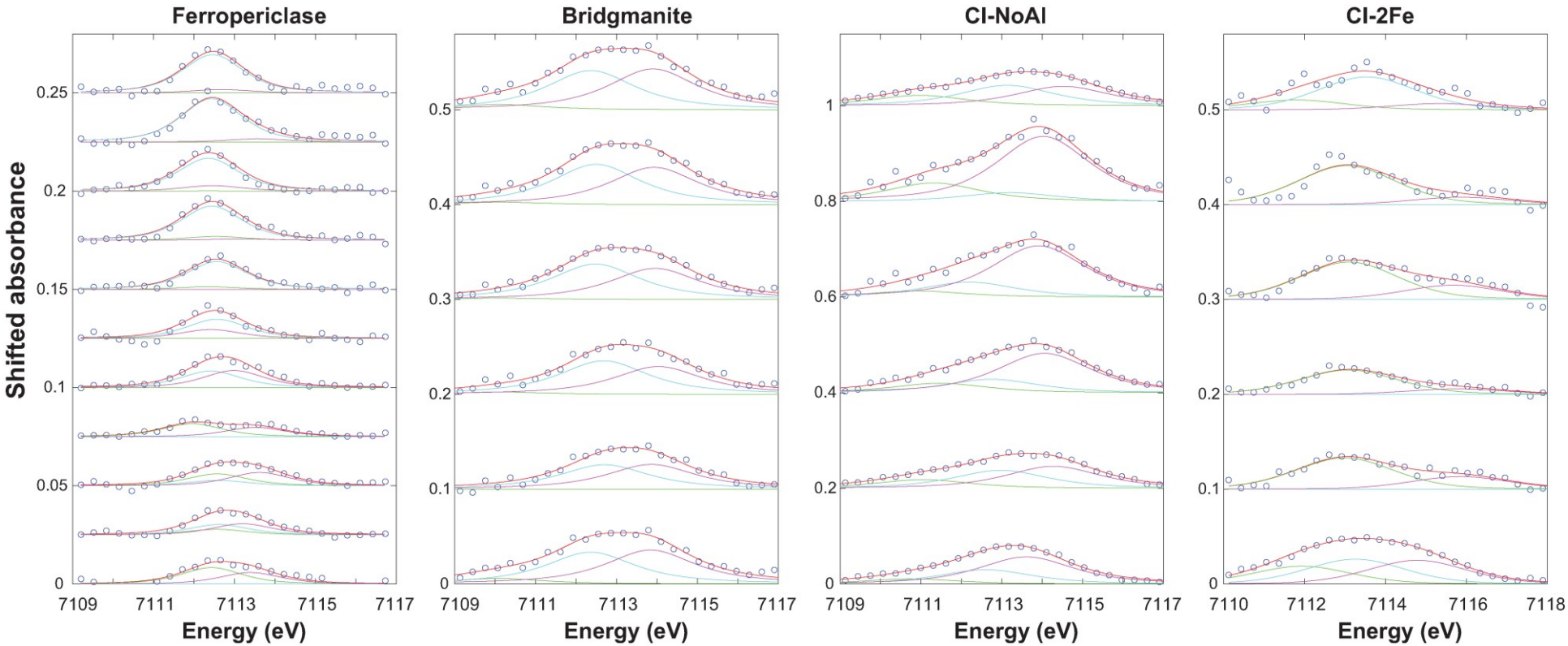

Figure S-4 Deconvolution of Fe-K pre-edges. Pre-edge features are located around 7110-7115 eV in the XANES spectra (Figs. S-1 and S-2). These features can be fitted by a sum of 3 contributions, plus a background. Then, the centroid positions are recalculated and compared with available references (Fig. 2). The pressure evolution of the energy position and intensity of pre-edge features in Fp and Bg can be used as a reference to discuss the redox state of Fe in our other samples containing a mixture of Fp and Bg.

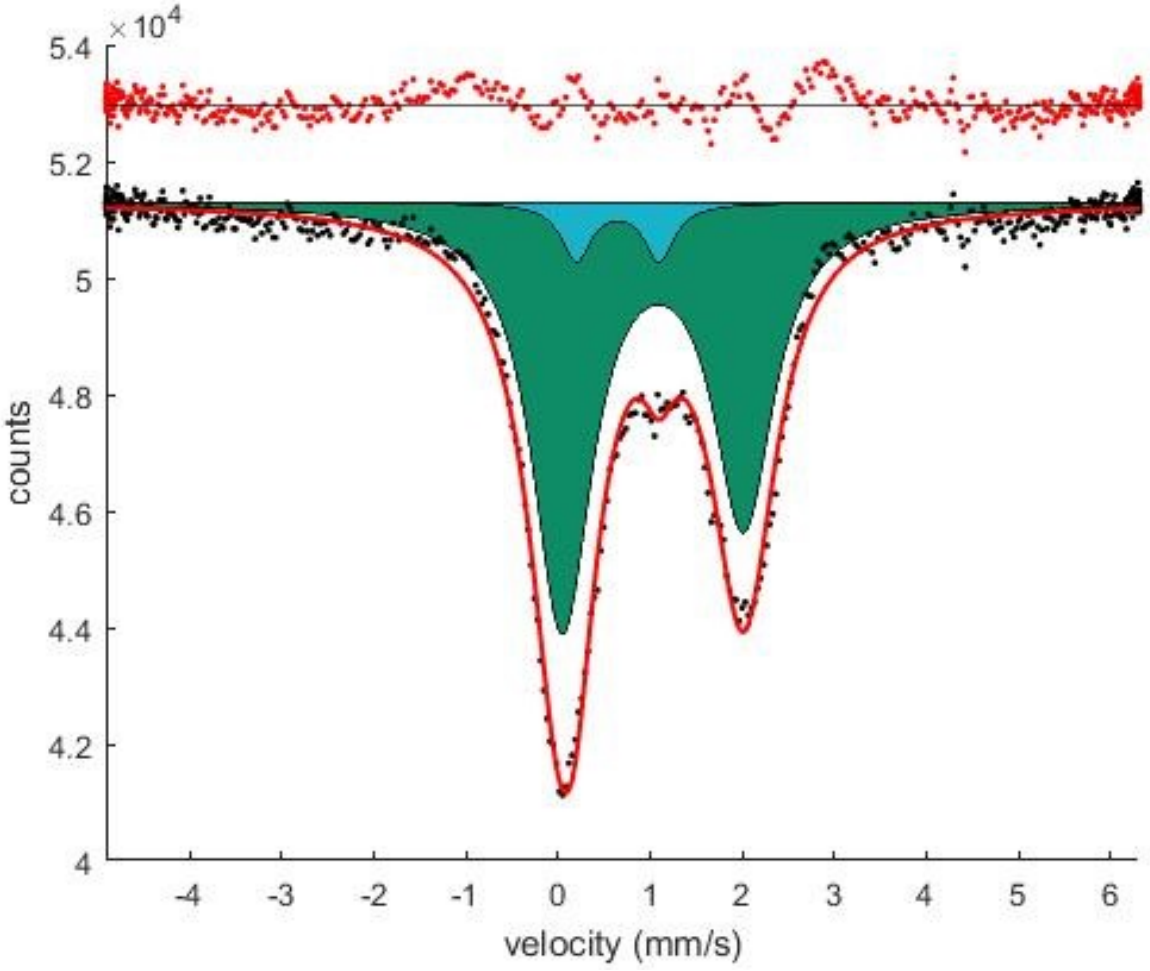

Figure S-5 Deconvolution of the SMS pattern of the glass starting material. The experimental spectrum (black dots) was recorded at 1 bar. According to previous works (Mao *et al.*, 2014; Murakami *et al.*, 2014), different contributions arise from high-spin Fe^{2+} (dark green doublet) and high-spin Fe^{3+} (light green doublet). The red line is the sum of these two contributions. The Fe^{3+} contribution points to #Fe^{3+} of 7.3 (0.5) %.

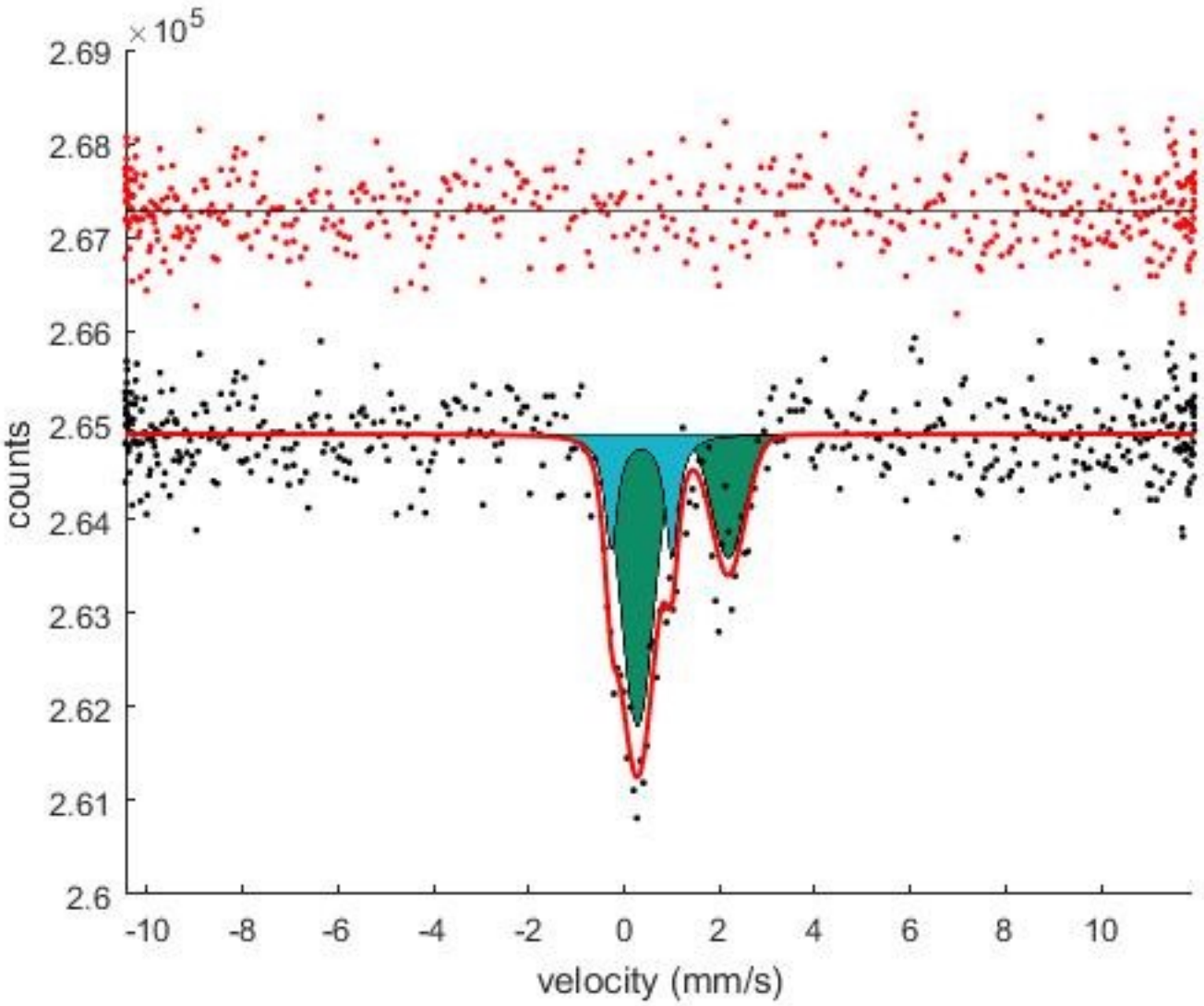

Figure S-6 SMS of the Bg reference compound (XANES). SMS measurement performed on the Bg sample recovered after the XANES experiments (Blue dots in Fig. 2). The spectrum presents two Fe contributions (Fe^{2+} HS and Fe^{3+} HS), yielding a #Fe^{3+} of 27(3) %.

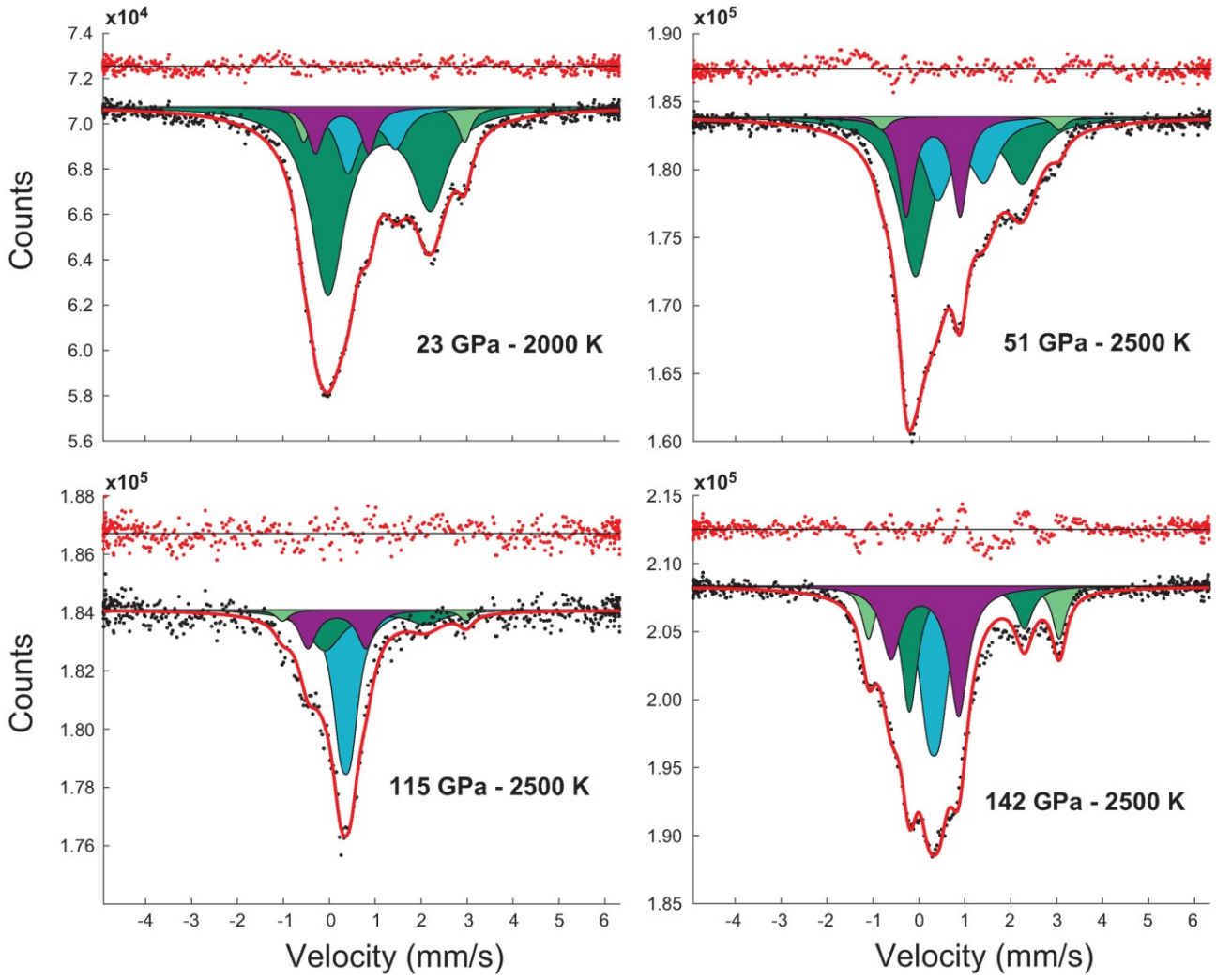

Figure S-7 Deconvolution of SMS patterns of our samples. Spectra were recorded at 300 K after synthesis at nominal pressures of 23 GPa **(upper-left)**, 51 GPa **(upper-right)**, 115 GPa **(lower-left)** and 142 GPa **(lower-right)**. The five different contributions found in the samples are high-spin Fe^{2+} and low-spin Fe^{2+} in Fp (blue doublet and singlet, respectively), high-spin Fe^{2+} (dark green doublet), intermediate-spin Fe^{2+} (light green doublet) and high-spin Fe^{3+} (purple doublet) in Bg.

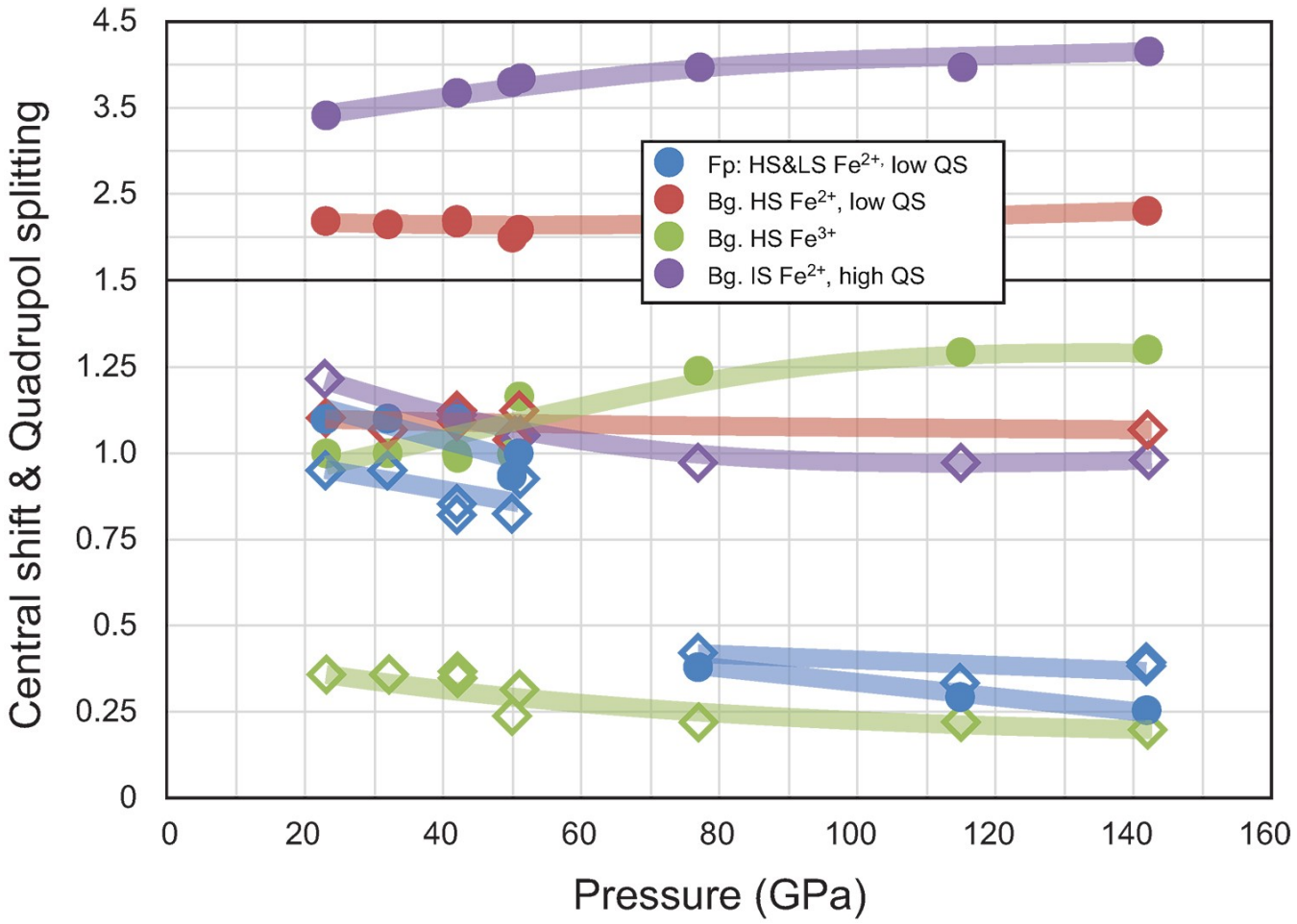

Figure S-8 Refined SMS parameters for transformed samples. CS (open lozenges) and QS (circles) are reported for the five Fe contributions: Two contributions for Fp are high-spin (low P) and low-spin (high P) Fe^{2+} (both reported in blue); three contributions for Bg are high-spin low-Q Fe^{2+} (red), high-spin Fe^{3+} (green) and intermediate-spin Fe^{2+} (purple). All QS and CS values were derived from previous works (McCammon *et al.*, 2008; Kantor *et al.*, 2009; Kupenko *et al.*, 2014).

Supplementary Information References

Andrault, D., Fiquet, G., Itié, J.P., Richet, P., Gillet, P., Häusermann, D., Hanfland, M. (1998) Thermal pressure in a laser-heated diamond-anvil cell: An x-ray diffraction study. *European Journal of Mineralogy* 10, 931-940.

Andrault, D., Munoz, M., Bolfan-Casanova, N., Guignot, N., Perrillat, J.P., Aquilanti, G., Pascarelli, S. (2010) Experimental evidence for perovskite and post-perovskite coexistence throughout the whole D'' region. *Earth and Planetary Science Letters* 293, 90-96.

Auzende, A.-L., Badro, J., Ryerson, F.J., Weber, P.K., Fallon, T.J., Addab, A., Siebert, J., Fiquet, G. (2008) Element partitioning between magnesium silicate perovskite and ferropericlase: New insights into bulk lower-mantle geochemistry. *Earth and Planetary Science Letters* 269, 164–174.

Badro, J., Fiquet, G., Guyot, F., Rueff, J.P., Struzhkin, V.V., Vanko, G., Monaco, G. (2003) Iron partitioning in Earth's mantle: Toward a deep lower mantle discontinuity. *Science* 300, 789-791.

Badro, J., Rueff, J.P., Vanko, G., Monaco, G., Fiquet, G., Guyot, F. (2004) Electronic transitions in perovskite: possible nonconvecting layers in the lower mantle. *Science* 305, 383-386.

Boujibar, A., Bolfan-Casanova, N., Andrault, D., Bouhifd, M.A., Trcera, N. (2016) Incorporation of Fe^{2+} and Fe^{3+} in bridgmanite during magma ocean crystallization. *American Mineralogist* 101, 1560-1570.

Fei, Y.W., Zhang, L., Corgne, A., Watson, H., Ricolleau, A., Meng, Y., Prakapenka, V. (2007) Spin transition and equations of state of (Mg, Fe)O solid solutions. *Geophysical Research Letters* 34.

Hennet, L., Cristiglio, V., Kozaily, J., Pozdnyakova, I., Fischer, H.E., Bytchkov, A., Drewitt, J.W.E., Leydier, M., Thiaudiere, D., Gruner, S., Brassamin, S., Zanghi, D., Cuello, G.J., Koza, M., Magazu, S., Greaves, G.N., Price, D.L. (2011) Aerodynamic levitation and laser heating: Applications at synchrotron and neutron sources. *European Physical Journal-Special Topics* 196, 151-165.

Irifune, T., Koizumi, T., Ando, J. (1996) An experimental study of the garnet-perovskite transformation in the system MgSiO3-Mg3Al2Si3O12. *Physics of the Earth and Planetary Interiors* 96, 147-157.

Irifune, T., Shinmei, T., McCammon, C.A., Miyajima, N., Rubie, D.C., Frost, D.J. (2010) Iron Partitioning and Density Changes of Pyrolite in Earth's Lower Mantle. *Science* 327, 193-195.

Kantor, I., Dubrovinsky, L., McCammon, C., Steinle-Neumann, G., Kantor, A., Skorodumova, N., Pascarelli, S., Aquilanti, G. (2009) Short-range order and Fe clustering in Mg1-xFexO under high pressure. *Physical Review B* 80.

Kesson, S.E., Fitz Gerald, J.D., Shelley, J.M. (1998) Mineralogy and dynamics of a pyrolite lower mantle. *Nature* 393, 252-255.

Kupenko, I., Dubrovinsky, L., Dubrovinskaia, N., McCammon, C., Glazyrin, K., Bykova, E., Ballaran, T.B., Sinmyo, R., Chumakov, A.I., Potapkin, V., Kantor, A., Ruffer, R., Hanfland, M., Crichton, W., Merlini, M. (2012) Portable double-sided laser-heating system for Mossbauer spectroscopy and X-ray diffraction experiments at synchrotron facilities with diamond anvil cells. *Review of Scientific Instruments* 83.

Kupenko, I., McCammon, C., Sinmyo, R., Cerantola, V., Potapkin, V., Chumakov, A.I., Kantor, A., Ruffer, R., Dubrovinsky, L. (2015) Oxidation state of the lower mantle: In situ observations of the iron electronic configuration in bridgmanite at extreme conditions. *Earth and Planetary Science Letters* 423, 78-86.

Kupenko, I., McCammon, C., Sinmyo, R., Prescher, C., Chumakov, A.I., Kantor, A., Ruffer, R., Dubrovinsky, L. (2014) Electronic spin state of Fe,Al-containing MgSiO3 perovskite at lower mantle conditions. *Lithos* 189, 167-172.

Lin, J.F., Vanko, G., Jacobsen, S.D., Iota, V., Struzhkin, V.V., Prakapenka, V.B., Kuznetsov, A., Yoo, C.S. (2007) Spin transition zone in Earth's lower mantle. *Science* 317, 1740-1743.

Mao, Z., Lin, J.F., Yang, J., Wu, J.J., Watson, H.C., Xiao, Y.M., Chow, P., Zhao, J.Y. (2014) Spin and valence states of iron in Al-bearing silicate glass at high pressures studied by synchrotron Mossbauer and X-ray emission spectroscopy. *American Mineralogist* 99, 415-423.

McCammon, C., Kantor, I., Narygina, O., Rouquette, J., Ponkratz, U., Sergueev, I., Mezouar, M., Prakapenka, V., Dubrovinsky, L. (2008) Stable intermediate-spin ferrous iron in lower-mantle perovskite. *Nature Geoscience* 1, 684-687.

McCammon, C.A. (1997) Perovskite as a possible sink for ferric iron in the lower mantle. *Nature* 387, 694-696.

Muñoz, M., De Andrade, V., Vidal, O., Lewin, E., Pascarelli, S., Susini, J. (2006) Redox and speciation micro-mapping using dispersive X-ray absorption spectroscopy: Application to iron in chlorite mineral of a metamorphic rock thin section. *Geochemistry Geophysics Geosystems* 7, Q11020.

Munoz, M., Pascarelli, S., Aquilanti, G., Narygina, O., Kurnosov, A., Dubrovinsky, L.S. (2008) Hyperspectral μ-XANES mapping in the diamond-anvil cell: analytical procedure applied to the decomposition of (Mg,Fe)-ringwoodite at the upper/lower mantle boundary. *High Pressure Research* 28, 665-673.

Munoz, M., Vidal, O., Marcaillou, C., Pascarelli, S., Mathon, O., Farges, F. (2013) Iron oxidation state in phyllosilicate single crystals using Fe-K pre-edge and XANES spectroscopy: Effects of the linear polarization of the synchrotron X-ray beam. *American Mineralogist* 98, 1187-1197.

Murakami, M., Goncharov, A.F., Hirao, N., Masuda, R., Mitsui, T., Thomas, S.M., Bina, C.R. (2014) High-pressure radiative conductivity of dense silicate glasses with potential implications for dark magmas. *Nature Communications* 5.

Murakami, M., Hirose, K., Sata, N., Ohishi, Y. (2005) Post-perovskite phase transition and mineral chemistry in the pyrolitic lowermost mantle. *Geophysical Research Letters* 32, L03304.

Nakajima, Y., Frost, D.J., Rubie, D.C. (2012) Ferrous iron partitioning between magnesium silicate perovskite and ferropericlase and the composition of perovskite in the Earth's lower mantle. *Journal of Geophysical Research-Solid Earth* 117.

Narygina, O., Dubrovinsky, L.S., Samuel, H., McCammon, C.A., Kantor, I.Y., Glazyrin, K., Pascarelli, S., Aquilanti, G., Prakapenka, V.B. (2011) Chemically homogeneous spin transition zone in Earth's lower mantle. *Physics of the Earth and Planetary Interiors* 185, 107-111.

Narygina, O., Mattesini, M., Kantor, I., Pascarelli, S., Wu, X., Aquilanti, G., McCammon, C., Dubrovinsky, L. (2009) High-pressure experimental and computational XANES studies of (Mg,Fe)(Si,Al)O_3 perovskite and (Mg,Fe)O ferropericlase as in the Earth's lower mantle. *Physical Review B* 79.

Piet, H., Badro, J., Nabiei, F., Dennenwaldt, T., Shim, S.H., Cantoni, M., Hebert, C., Gillet, P. (2016) Spin and valence dependence of iron partitioning in Earth's deep mantle. *Proceedings of the National Academy of Sciences of the United States of America* 113, 11127-11130.

Potapkin, V., Chumakov, A.I., Smirnov, G.V., Celse, J.P., Ruffer, R., McCammon, C., Dubrovinsky, L. (2012) The Fe-57 Synchrotron Mossbauer Source at the ESRF. *Journal of Synchrotron Radiation* 19, 559-569.

Prescher, C., Langenhorst, F., Dubrovinsky, L.S., Prakapenka, V.B., Miyajima, N. (2014) The effect of Fe spin crossovers on its partitioning behavior and oxidation state in a pyrolitic Earth's lower mantle system. *Earth and Planetary Science Letters* 399, 86-91.

Prescher, C., McCammon, C., Dubrovinsky, L. (2012) MossA: a program for analyzing energy-domain Mossbauer spectra from conventional and synchrotron sources. *Journal of Applied Crystallography* 45, 329-331.

Sakai, T., Ohtani, E., Terasaki, H., Sawada, N., Kobayashi, Y., Miyahara, M., Nishijima, M., Hirao, N., Ohishi, Y., Kikegawa, T. (2009) Fe-Mg partitioning between perovskite and ferropericlase in the lower mantle. *American Mineralogist* 94, 921-925.

Shim, S.-H., Grocholski, B., Ye, Y., Alp, E.E., Xu, S., Morgan, D., Meng, Y., Prakapenka, V.B. (2017) Stability of ferrous-iron-rich bridgmanite under reducing midmantle conditions. *Proceedings of the National Academy of Sciences of the United States of America* 114, 6468-6473.

Sinmyo, R., Hirose, K. (2013) Iron partitioning in pyrolitic lower mantle. *Physics and Chemistry of Minerals* 40, 107-113.

Sinmyo, R., Hirose, K., Muto, S., Ohishi, Y., Akira, Y. (2011) The valence state and partitioning of iron in the Earth's lowermost mantle. *journal of Physical Research* In Press.

Wilke, M., Farges, F., Petit, P.E., Brown, J.G.E., Martin, F. (2001) Oxidation state and coordination of Fe in minerals: An Fe K-XANES spectroscopic study. *American Mineralogist* 86, 714-730.

Wood, B.J., Rubie, D.C. (1996) The effect of alumina on phase transformations at the 660-kilometer discontinuity from Fe-Mg partitioning experiments. *Science* 273, 1522-1524.